24th International Congress of Theoretical and Applied Mechanics

In Situ Observation Of Strained Bands And Ductile Damage In Thin AA2139-T3 Alloy Sheets

Ante Buljac[a,b], Thibault Taillandier-Thomas[a,b], Thilo F. Morgeneyer[b], Lukas Helfen[c,d], Stéphane Roux[a], François Hild[a,*]

[a]*Laboratoire de Mécanique et Technologie (LMT), ENS Cachan/CNRS/Université Paris-Saclay*
61 avenue du Président Wilson, 94235 Cachan, France
[b]*MINES ParisTech, PSL Research University, MAT-Centre des matériaux, CNRS UMR 7633, BP 87, 91003 Evry, France*
[c]*ANKA/Institute for Photon Science and Synchrotron Radiation, Karlsruhe Institute of Technology (KIT), D-76131 Karlsruhe, Germany*
[d]*European Synchrotron Radiation Facility (ESRF), F-38043 Grenoble, France*

Abstract

The interactions between plasticity and damage mechanisms are not clearly established concerning the fracture of ductile sheet materials (*e.g.,* flat to slant transition). The question addressed herein is to elucidate which mechanism is responsible for localized phenomena leading to the final failure. A mechanical test carried out on a notched plate made of 2139-T3 aluminum alloy is imaged thanks to synchrotron laminography at micrometer resolution. Ductile damage (*i.e.,* void nucleation, growth and coalescence) is analyzed via reconstructed volumes. Although the low volume fraction of secondary phases in the tested alloy is challenging, digital volume correlation is also utilized to measure displacement fields and estimate strain fields in the bulk of the alloy during the whole test. In the first part of this study, the resolution of the measurement technique is assessed under such conditions. Then strained bands are shown to occur very early on in what will be the slant region of the fracture path. Conversely, damage grows at very late loading steps.

1. Introduction

Ductile damage generally has three phases, namely, void nucleation, growth and coalescence. Unlike fracture mechanics, modeling such mechanisms calls for micromechanics-based approaches with more physical input. Various damage models successfully deal with high stress triaxialities [1,2,3]. However, lower triaxialities (*e.g.,* ductile failure in shear loading) are challenging [4,5]. Failure mechanisms responsible for cracking under such conditions are still poorly understood and quantified.

A typical example of the afore-mentioned challenges are flat-to-slant failures of thin samples under mode I loading [6,7,8,9,10,11]. In these specimens the crack starts to propagate perpendicular to the loading direction. Later on, it

---

* Corresponding author. Fax: +33-1-47-40-22-40.
E-mail address: hild@lmt.ens-cachan.fr (François Hild).

continues to propagate in a slant manner. This phenomenon may lead to reduced toughness compared with pure mode I opening. Numerically it has been shown that slant cracks propagate in plane strain conditions with respect to the crack propagation direction [12] and dissipate less energy during tearing than a flat crack [11]. The first observation has been experimentally confirmed [13]. The simultaneous match of load/displacement response and propagation path still remains very challenging. Shear bands as driving force for such type of failure have been theoretically studied [14]. It was found that materials showing a sharp vertex on the yield surface are prone to strain localization. Similarly, damage growth and (self)heating due to plastic flow (*i.e.,* thermal softening) are also mentioned as possible causes for localized strain patterns in materials.

Tomography has been successfully utilized to study bulk failure mechanisms in structural alloys [15]. Yet, tomography is by construction limited to cylinders where representative sheet loading conditions cannot be easily prescribed. Synchrotron radiation computed laminography [16,17,18] allows damage processes to be analyzed *in situ* in sheet-like specimens [10]. It is also possible to apply boundary conditions of engineering relevance. Further, thanks to Digital Volume Correlation (DVC), *e.g.,* with a global formulation [19], the bulk displacement fields can be measured. Hence, strain and damage interactions can be quantitatively assessed in naturally developing plastic bands on the order of several millimeters in front of the notch root [20,21] at micrometer resolutions.

In the present work a CT-like sample made of aeronautical aluminum alloy 2139 is monitored *in situ* by using laminography. It was shown that for another alloy (*i.e.,* AA2198-T8) early strained bands form before any sign of damage growth is detected in a Region of Interest (ROI) placed $\approx 800~\mu m$ ahead of the notch root [21]. The same type of analysis is reported herein for AA2139-T3, which contains a significant initial porosity (*i.e.,* ≈ 0.3 %) in comparison with the previous case, and displays a more progressive work hardening. The paper is structured as follows. The material properties, mechanical setup and laminography imaging technique are first introduced. The basic principles of DVC incorporating strain uncertainty assessments are discussed next. The results and conclusions are finally presented.

2. Experimental setup

The material of the CT-like specimen studied herein (AA 2139) is produced by Constellium C-Tech and represents the latest generation of Al-Cu-Mg alloys. The yield strength is ≈ 320 MPa and the ultimate tensile strength is ≈ 450 MPa. The chosen T3 heat treatment is responsible for the material high work hardening. The intermetallic particle volume fraction is found to be ≈ 0.45 % while the initial porosity is of the order of 0.3 vol %. The low volume fraction of secondary phases makes this material very challenging for DVC [20]. The material processing directions are the rolling direction (L), the transverse direction (T) and the short-transverse direction in the through thickness (S). In the experiment, the loading is applied in the T-direction and the L-direction corresponds to that of crack propagation. More details on the material properties can be found in Refs. [22,23].

Synchrotron radiation computed laminography enables laterally extended 3D objects to be imaged in a non-destructive way [24,25,26,27]. This technique is of particular interest in the field of mechanics of materials since using sheet-like samples allows a wide range of engineering relevant boundary conditions to be prescribed. The characteristic feature of laminography is the inclination of the sample with respect to the beam that can assume an angle θ different from 90°, while tomography is limited to 90° angle during the scanning procedure.

The testing machine with a stepwise loading procedure is shown in Fig. 1(a) without the anti-buckling system. The dimensions of the CT-like specimen are $60 \times 70 \times 1$ mm (Fig. 1(b)). Electrical discharge machining is utilized to create a notch radius of 0.17 mm. The corresponding ligament is 24-mm in length. After applying each loading step (Fig. 1(c)), the object is scanned while rotating about the laminograph axis. The collected radiographs are used to reconstruct the 3D volume by using a filtered-back-projection algorithm [28]. The crack size is manually estimated on the reconstructed volumes (Fig. 1(d)) and the crack mouth opening displacement (CMOD) corresponds to the screw displacement. The beamline ID19 of the European Synchrotron Radiation Facility (Grenoble, France) with a 25 keV monochromatic beam allows a spatial resolution of 0.7 μm per voxel (which requires 1500 projections per scan) to be obtained. The rotation axis inclination angle is chosen to be $\theta \approx 65°$.
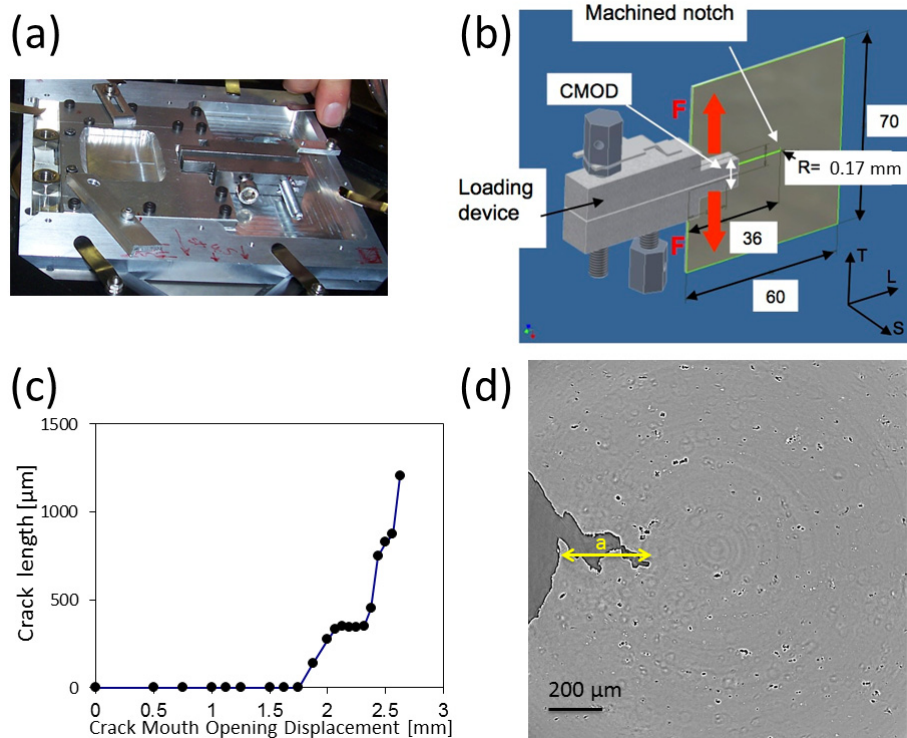
Figure 1: (a) Photograph of the specimen, loading device and anti-buckling frame mounted onto the laminography specimen holder. (b) Drawing of the flat (*i.e.,* 1-mm thick) CT-like specimen and loading device. (c) Measured crack length versus CMOD curve (every dot on the curve corresponds to one load increment and corresponding scan). (d) 2D section of reconstructed laminography data at mid thickness when CMOD = 2.13 mm

3. Digital Volume Correlation

The DVC procedure utilized herein is an extension of 2D global Digital Image Correlation[29,30]. The reconstructed volume is based on X-ray absorption contrast encoded in 8-bit deep gray levels. DVC consists of measuring the displacement field **u** for two scans, namely, $f(\mathbf{x})$ in reference and $g(\mathbf{x})$ in the deformed configurations at voxels **x** such that the gray level conservation reads

$$f(\mathbf{x}) = g(\mathbf{x} + \mathbf{u}(\mathbf{x})) \tag{1}$$

Because of acquisition noise, reconstruction artifacts[31], and the registration procedure itself[32] ideal match is not achieved. Consequently, Equation (1) is not strictly satisfied. The solution consists of minimizing the gray level residual

$$\rho(\mathbf{x}) = f(\mathbf{x}) - g(\mathbf{x} + \mathbf{u}(\mathbf{x})) \tag{2}$$

by considering its L2-norm over the considered Region of Interest (ROI) with respect to kinematic unknowns. Since global DVC[19] is carried out in this work, the measured displacement field is C_0-continuous over the ROI. A weak formulation based on 8-noded cubes (C8) with trilinear shape functions is chosen. A multiscale Gauss-Newton scheme is implemented to conduct the minimization procedure[19]. The result of a DVC analysis is the 3D displacement field inside the ROI. The mean deformation gradient over each C8 element is used to obtain the Green-Lagrange strain tensor, and its second invariant is reported hereafter.

The measurement resolution is evaluated by the standard deviation of the measured displacement and calculated strain fields for two scans in the reference configuration. For the chosen element size (*i.e.,* edge length for all three directions, $\ell = 32$ voxels or 22 μm), the standard equivalent strain resolution is equal to 0.5 %. This value represents the limit below which the estimated strain levels are not trustworthy.

The present work aims at investigating the development of plastic strains and damage in the tearing experiment on AA2139-T3. It is chosen to show both fields simultaneously as depicted in Fig. 2. The study focuses on a region (whose outer face is situated 1080 μm ahead of the notch root and normal to the crack propagation direction, see Fig. 2(a)) where the crack is slanted. The 3D rendering of von Mises strain field is shown in Fig. 2(b) when DVC is run between the undeformed state (*i.e.,* CMOD = 0.0 mm) and when CMOD = 1.5 mm. Figure 2(c) shows a section for which the equivalent strain field is laid over the microstructure as revealed by laminography. In particular, the porosities and secondary particles can be observed. Both fields are displayed in the reference configuration.
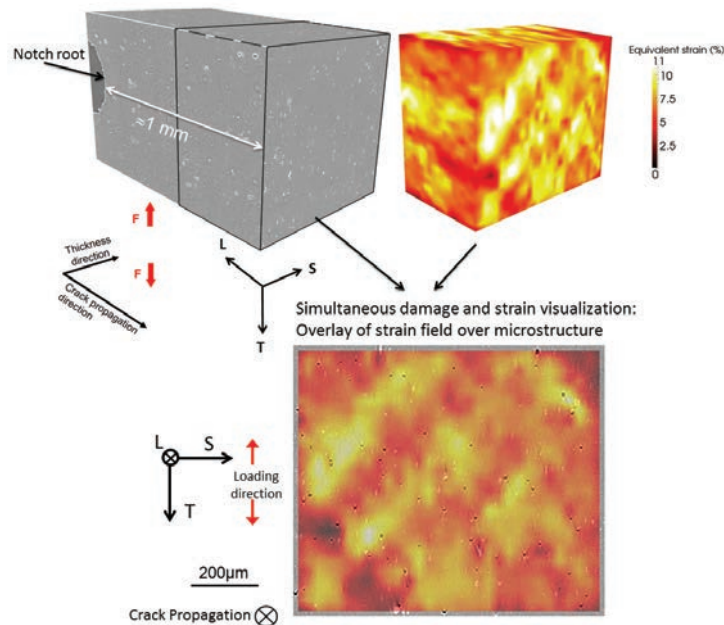

Figure 2: (a) 3D rendering of the initial microstructure and the chosen ROI. (b) 3D rendering of the equivalent strain field in the extracted volume when CMOD = 1.5 mm. (c) 2D overlay of strain field over the initial microstructure

4. Results and conclusions

The representation shown in Fig. 2(c) is now reported for different load steps and corresponding *incremental* correlations (Fig. 3), namely, the underlying reference microstructure (*i.e.,* at step n) is shown with an overlay of the incremental von Mises equivalent strain field for DVC analyses between steps n and $n + 1$.

The equivalent strain field for a load increment starting from the unloaded state to CMOD = 1.5 mm is shown in Fig. 3(a). For this first load increment there is no crack that has initiated from the initial notch. A heterogeneous distribution of equivalent strains is observed with an average level $\approx$ 10 %. Several parallel slant bands have formed at this relatively early stage of loading. Further, no clear correlation between the underlying voids, particles and the strained bands is found. The strain levels within the bands is about twice as high as in the zones outside the bands. Two particular voids of the microstructure are encircled in the considered 2D section. They will be followed for the subsequent load increments and will serve as an absolute reference, thereby enabling the motions of the strained bands to be studied with respect to the underlying microstructure.

An overlay of the *incremental* equivalent strain field between CMOD = 1.5 mm and CMOD = 2.0 mm is shown over the underlying microstructure corresponding to CMOD = 1.5 mm in Fig. 3(b). The upper strained band of the first analysis is the most active in the present case whereas the other two are less active. When the strained bands are compared with the underlying microstructure, it is observed that the bands are motionless in the material frame (*i.e.,*
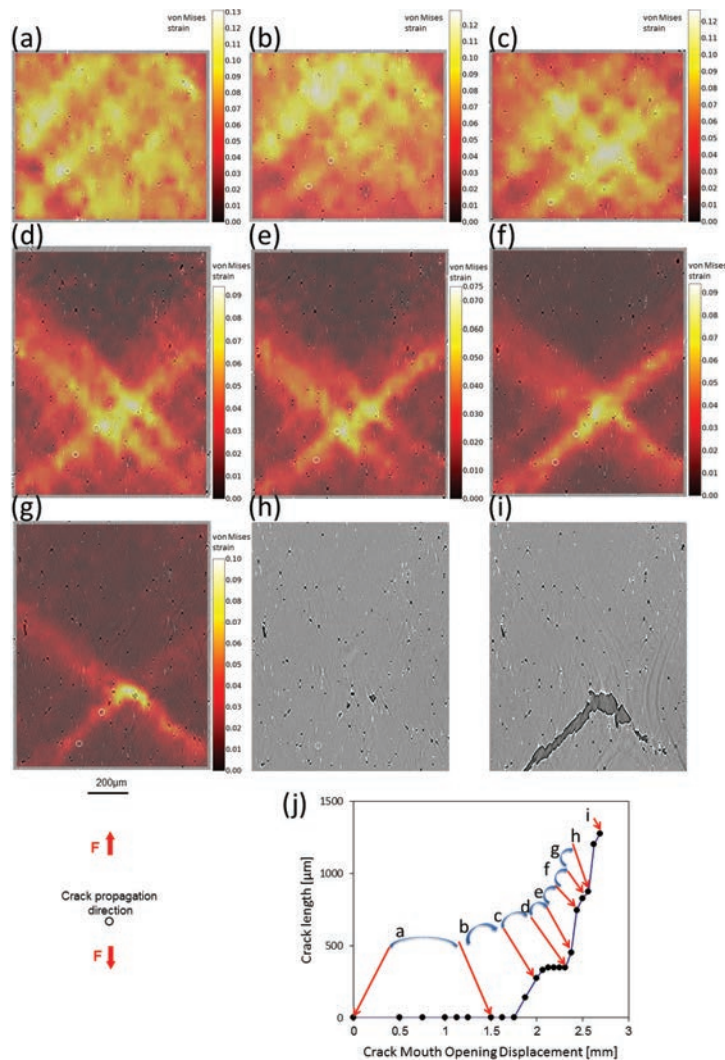
Figure 3: Overlay of incremental equivalent strain fields (half transparent) over the microstructure 1080 μm ahead of the notch root. (a)-(g) 2D sections of laminography data and equivalent strain fields. The microstructure is shown in state *n* for incremental DVC analyses between states *n* and *n* + 1. Two reference voids are encircled in white on the microstructure for every load step. (h), (i) Microstructure showing damage and the final crack path. (j) Load steps corresponding to the displayed sections

the same voids and particles are found within the bands). The void and particle changes are very limited even though, at this load step, the main crack is already propagating from the notch root.

Figure 3(c) shows the next load increment from CMOD = 2.0 mm to 2.3 mm. The two upper strained bands are now active. The lower of the two bands is again situated above the two encircled voids as for the first analyzed step (see Fig. 3(a)). It is worth noting that there is another very active band oriented normal to the two previous ones, and even more slant crossing bands are active in the center of the ROI. A "waffle-like" strain pattern forms with separations between the strained bands on the order of 150-250 μm. No noticeable void or particle growth occurs during this load increment.

In order to follow the two remarkable voids, the extracted volume has been symmetrically increased in the loading direction. Even though a small step between CMOD = 2.3 mm and 2.38 mm is considered, it leads to high local incremental strains as the crack approaches the ROI. Only one strained band is active (Fig. 3(d)) spanning from the

lower left part to the upper right part and located above the two encircled voids. Two other parallel strained bands are active normal to this band. The strain field is now substantially more localized than in Fig. 3(c). For the next load step (from CMOD = 2.38 mm to 2.44 mm, see Fig. 3(e)) a very similar strain pattern is observed. Virtually no damage growth is seen in the microstructure.

Figure 3(f) shows the same strained band from the lower left to the upper right corner of the image. Only one out of the two bands normal to this one (*i.e.,* the upper band) is still active. The latter is particularly active in the lower part of the ROI. At these late stages of loading there still are several bands that have undergone tens of per cent of strain rather than the single active strained band that could have been anticipated. The next analysis from CMOD = 2.44 mm to 2.5 mm is the last one for which trustworthy registration could be obtained (Fig. 3(g)). From the analysis of the underlying microstructure it is concluded that damage has grown notably.

Figure 3(h) only shows the microstructure when CMOD = 2.5 mm. Voids in the region where the two strained bands cross further grow. The final crack path is shown in Fig. 3(i) when CMOD = 2.63 mm. A roof top pattern is seen, which has not fractured the full section yet. From the present analyses it is concluded that the crack has followed the second slant strained band that is present from the very early loading stage and onward. The two voids that had been encircled in the previous load increments have contributed to the final fracture surface.

To summarize, the main findings of the present study are:

- several parallel, crossing and slant strained bands are observed from very early stages of loading on,
- intermittent activity of incremental strain fields, and strained bands with high equivalent strain levels (*i.e.,* 0.10 or more) may become inactive and others become active later on,
- stable spatial location of bands compared to the microstructure,
- strained band spacing of the order of 150-250 μm, and ratio of equivalent strain within and outside bands is $\approx$ 1.5-2,
- in the analyzed region of interest, substantial void growth is not detected at micrometer resolution before the occurrence and development of strained bands,
- the final failure takes place along one of the bands that was already active since the very beginning of the loading history,
- the mechanisms at play for strain concentration differ from damage softening.

The interested reader will find additional discussions on the same experiment, and some modeling effort to describe the reported observations in Ref.[36].

Acknowledgements

References

1. Gurson A. Continuum Theory of Ductile Rupture by Void Nucleation and Growth: Part I - Yield Criterion and Flow Rules for Porous Ductile Media. *J Eng Mat Techn* 1977;**99**:2-15.
2. Tvergaard V, Needleman A. Analysis of the cup-cone fracture in a round tensile bar. *Acta Metall* 1984;**32(1)**:157-169.
3. Lemaitre J. *A Course on Damage Mechanics.* Berlin (Germany): Springer-Verlag; 1992.
4. Faleskog J, Barsoum I. Tension-torsion fracture experiments-Part I: Experiments and a procedure to evaluate the equivalent plastic strain. *Int J Solids Struct* 2013;**50(25-26)**:4241-4257.
5. Papasidero J, Doquet V, Mohr D. Determination of the Effect of Stress State on the Onset of Ductile Fracture Through Tension-Torsion Experiments. *Exp Mech* 2014;**54(2)**:13–151.
6. Mahgoub E, Deng X, Sutton MA. Three dimensional stress and deformation fields around flat and slant cracks under remote mode I loading conditions. *Eng Fract Mech* 2003;**70**:2527-2542.
7. Bron F, Besson J, Pineau A. Ductile rupture in thin sheets of two grades of 2024 aluminum alloy. *Mat Sci Eng* 2004;**A380(1-2)**:356-364.
8. Asserin-Lebert A, Besson J, Gourgues AF. Fracture of 6056 aluminum sheet materials: effect of specimen thickness and hardening behavior on strain localization and toughness. *Mat Sci Eng* 2005;**A395(1-2)**:186-194.
9. Lan W, Deng X, Sutton MA, Chen C. Study of slant fracture in ductile materials. *Int J Fract* 2006;**141**:469-496.
10. Morgeneyer T, Helfen L, Sinclair I, Proudhon H, Xu F, Baumbach T. Ductile crack initiation and propagation assessed via in situ synchrotron radiation computed laminography. *Scripta Mat* 2011;**65**:1010-1013.

11. Besson J, McCowan C, Drexler E. Modeling flat to slant fracture transition using the computational cell methodology. *Eng Fract Mech* 2013;**104**:80-95.
12. Bron F, Besson J. Simulation of the ductile tearing for two grades of 2024 aluminum alloy thin sheets. *Eng Fract Mech* 2006;**73(11)**:1531-1552.
13. Buljac A, Taillandier-Thomas T, Morgeneyer T, Helfen L, Roux S, Hild F. Slant strained band development during flat to slant crack transition in AA 2198 T8 sheet: In situ 3D measurements. *Int J Fract* 2016;**200(1)**:49-62.
14. Needleman A, Tvergaard V. Analyses of Plastic Flow Localization in Metals. *Appl Mech Rev* 1992;**45(3S)**:S3-S18.
15. Maire E, Withers PJ. Quantitative X-ray tomography. *Int Mat Rev* 2014;**59(1)**:1-43.
16. Altapova V, Helfen L, Myagotin A, Hänschke D, Moosmann J, Gunneweg J, Baumbach T. Phase contrast laminography based on Talbot interferometry. *Optics Expr* 2012;**20**:6496-6508.
17. Helfen L, Baumbach T, Mikulík P, Kiel D, Pernot P, Cloetens P, Baruchel J. High-resolution three-dimensional imaging of flat objects by synchrotron-radiation computed laminography. *Appl Phys Lett* 2005;**86(7)**:071915.
18. Helfen L, Baumbach T, Cloetens P, Baruchel J. Phase contrast and holographic computed laminography. *Appl Phys Lett* 2009;**94**:104103.
19. Roux S, Hild F, Viot P, Bernard D. Three dimensional image correlation from X-Ray computed tomography of solid foam. *Comp Part A* 2008;**39(8)**:1253-1265.
20. Morgeneyer TF, Helfen L, Mubarak H, Hild F. 3D Digital Volume Correlation of Synchrotron Radiation Laminography Images of Ductile Crack Initiation: An Initial Feasibility Study. *Exp Mech* 2013;**53(4)**:543-556.
21. Morgeneyer TF, Taillandier-Thomas T, Helfen L, Baumbach T, Sinclair I, Roux S, Hild F. In situ 3-D observation of early strain localization during failure of thin Al alloy (2198) sheet. *Acta Mat* 2014;**69**:78-91.
22. Morgeneyer TF, Starink M, Sinclair I. Evolution of voids during ductile crack propagation in an Al-alloy sheet toughness test studied by micro-computed tomography. *Acta Mat.* 2008;**56**:1671-1679.
23. Morgeneyer TF, Besson J, Proudhon H, Starink M, Sinclair I. Experimental and numerical analysis of toughness anisotropy in AA2139 Al-alloy sheet *Acta Mat.* 2009;**57**:3902-3915.
24. Helfen L, Myagotin A, Pernot P, DiMichiel M, Mikulík P, Berthold A, Baumbach T. Investigation of hybrid pixel detector arrays by synchrotron-radiation imaging. *Nucl Inst Meth Phys Res A* 2006;**563**:163-166.
25. Maurel V, Helfen L, N'Guyen F, Köster A, DiMichiel M, Baumbach T, Morgeneyer TF. Three-dimensional investigation of thermal barrier coatings by synchrotron radiation computed laminography. *Scripta Mat* 2012;**66**:471-474.
26. Bull DJ, Helfen L, Sinclair I, Spearing SM, Baumbach T. A Synthesis of Multi-Scale 3D X-ray Tomographic Inspection Techniques for Assessing Carbon Fibre Composite Impact Damage. *Compos Sci Technol* 2013;**75**:55-61.
27. Reischig P, Helfen L, Wallert A, Baumbach T, Dik J. Non-invasive, threedimensional X-ray imaging of paint layers. *Appl Phys A* 2013;**111**:983-995.
28. Myagotin A, Voropaev A, Helfen L, Hänschke D, Baumbach T. Efficient Volume Reconstruction for Parallel-Beam Computed Laminography by Filtered Backprojection on Multi-Core Clusters. *IEEE Trans Image Process* 2013;**22(12)**:5348-5361.
29. Besnard G, Hild F, Roux S. "Finite-element" displacement fields analysis from digital images: Application to Portevin-Le Châtelier bands. *Exp Mech* 2006;**46**:789-803.
30. Hild F, Roux S. Comparison of local and global approaches to digital image correlation. *Exp Mech* 2012;**52(9)**:1503-1519.
31. Xu F, Helfen L, Baumbach T, Suhonen H. Comparison of image quality in computed laminography and tomography. *Optics Expr* 2012;**20**:794-806.
32. Leclerc H, Périé JN, Roux S, Hild F. Voxel-scale digital volume correlation. *Exp Mech* 2011;**51(4)**:479-490.
33. Réthoré J, Tinnes JP, Roux S, Buffière JY, Hild F. Extended three-dimensional digital image correlation (X3-DIC). *CR Mécanique* 2008;**336**:643-649.
34. Bouterf A, Roux S, Hild F, Adrien J, Maire E, Meille S. Digital volume correlation applied to X-ray tomography images from spherical indentation tests on lightweight gypsum. *Strain* 2014;**50(5)**:444-453.
35. Needleman A, Rice J. Limits to Ductility Set by Plastic Flow Localization. In: *General Motors Research Laboratories Symposium, Mechanics of Sheet Metal Forming*. Plenum Press; 1977. p. 237-267.
36. Morgeneyer TF, Taillandier-Thomas T, Buljac A, Helfen L, Hild F. On strain and damage interactions during tearing: 3D in situ measurements and simulations for a ductile alloy (AA2139-T3). *J Mech Phys Solids* 2016, **96**:550-571.